LEHIGH UNIVERSITY
DEPARTMENT OF COMPUTER SCIENCE AND ENGINEERING

CSE 498: Computer Vision

Final Project Report

Lung Segmentation and its importance in Disease classification

---

Advisor: Aparna Bharti

BETHLEHEM, PENNSYLVANIA, NOVEMBER 2022

Contents

1 Member list & Workload

No.	Full name	Percentage of work
1	Abhishek Srivastava	50%
2	Kaushik Jagani	50%

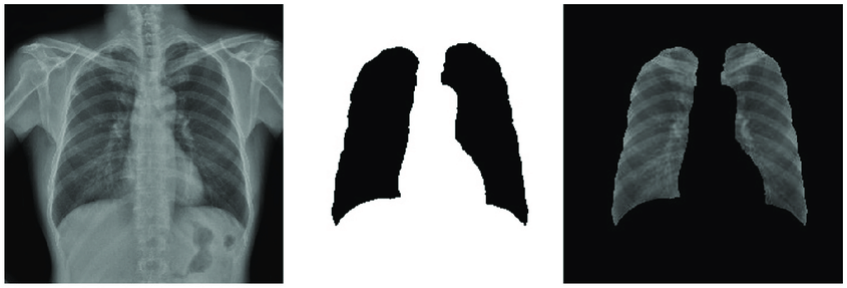

Figure 1: Lung Segmentation

2 Problem Statement

Surgery planning, disease diagnosis, and prognosis all depend on being able to accurately identify organ boundaries in medical pictures. The technique of correctly separating the regions and borders of the lung field from surrounding thoracic tissue is known as lung segmentation, and it is a crucial first step in pulmonary image processing for many clinical decision support systems. In this study, we suggest an approach based on deep learning for segmenting the lung regions in chest X-rays and eventually classify diagnosis of patients using the segmented image as an input to the classifier model. Figure 1 shows basic lung segmentation outputs.

3 Motivation

Additional computer analysis of concerned anatomical regions is available when lung fields are accurately defined. This enables the extraction of clinically relevant features that can be used to train a machine learning algorithm for the detection of disease and anomalies. In order to improve the caliber of care and patient outcomes, these computational tools can assist physicians in making rapid, precise diagnoses. For chest disorders such lung cancer, pulmonary edema (fluid in the lung), pleural effusion (fluid between the lung and chest cavity), pneumonia (infection by bacteria, viruses, fungus, or parasites), and tuberculosis, chest radiography is the most often used diagnostic imaging test (bacterial infection). Chest disorders cause more than 10 million deaths worldwide each year. According to a survey, 6.3 million people died from ischemic heart disease [3], 4.3 million from lower respiratory infections, 2.2 million from chronic obstructive pulmonary disease, 2 million from tuberculosis [6], and 0.9 million from other chest disorders in 1990 (lung cancer) [2]. Many treatments are only effective in the early, symptomless stages of most diseases. For accurate lung CT image analysis, such as lung cancer detection, lung image segmentation is a necessary step. The change in the visual extent of the disease over time is an essential measure of response to therapy and a predictor of death, and it can be used to quantify the progression, regression, or stagnation of lung disease. Additionally, segmented lungs can be employed for image registration, particularly in 3-D scans. As a result, the radiologists will be able to assess the volumetric changes in the lungs and determine the percentage of the patients' healthy parenchyma region that has been functionally reduced.

4 Literature Review

The delineation of anatomical features and other regions of interest is automated or made easier with the help of medical picture segmentation, which is essential in many imaging applications. Since the last ten years, the segmentation of lung fields in chest X-rays (CXR) have gained a lot of attention in the literature. For this work, a thorough review of lung segmentation methods for chest radiographs was conducted.

Much of the works mentioned used the JSRT dataset [1] as their image database. The Japanese Society of Radiological Technology (JSRT) created a database of chest radiographs (with and without lung nodules) and made it available to the public along with its ground truth clinical data. Only two studies, as far as we are aware, have used portable radiography of the chest. This demonstrates the lack of research on portable chest radiographs, which are extremely crucial, especially for critically ill patients.

Early segmentation techniques for CXR were divided into four groups: rule-based techniques, pixel classification-based techniques, deformable model-based techniques, and hybrid techniques [5]. A rule-based scheme includes a series of actions, tests, and rules. The techniques include local thresholding, region growth, edge and ridge detection, morphological procedures, fitting of geometrical models, functions, and dynamic programming. Pixel classification-based technique, on the other hand, is more generic and basically models the intensities of the picture and classifies the pixels into lung field or background. The rule-based scheme is presented using Bezier interpolation of prominent control points. used the fuzzy clustering method (FCM)-based scheme, and one of their comparison outcomes was the post-processed pixel classification approach.

Although it has numerous limitations when used to apply towards discovering appropriate groups in data analysis tasks, the FCM method[9] is the most well-known. To have a more reliable FCM, several researchers have attempted to change the fundamental goal function. FCM has been utilized with some success in the soft or fuzzy segmentation in medical imaging of chest CT, chest MRI, and brain MRI, even though the perfect segmentation of an image is often application dependent. The authors' motivation to use the FCM in their study came from the ease with which the borders of the lung or brain could be seen in CT and MRI images thanks to the unique bone and cell tissue. In their study, Rastgarpour et al.[14] merged a local region-based level set approach with a version of fuzzy clustering in order to segment a few modalities and body parts, including the lung, Gong et al. [13] applied FCM with spatial constraints to segment the lung for CXR. The literature also contains a few publications on additional FCM-based CXR applications. In their implementation of the algorithm for pneumonia identification, Parveen et al. also employed feature vectors to cluster feature data for atypicality detection by segmenting cardiac information (size, contour, and shape). The inhomogeneities of X-Ray imaging are mostly to blame for the paucity of work on lung segmentation for CXR utilizing FCM. FCM is difficult to utilize as a segmentation technique because of the sharp edges at the clavicle and rib cage regions as well as the intensity fluctuation around the lung area.

The deformable model-based approaches represent a recently developed system that has been thoroughly investigated and applied in medical picture segmentation. Lung area segmentation has been effectively used to this shape-flexibility model, Active Shape Model (ASM) and Active Appearance Model (AAM) [11]. But both have several drawbacks and restrictions, such as the need for manual initialization and supervision when changing parameters, which results in very variable solutions. The creation of the hybrid scheme aims to improve segmentation outcomes by combining the strategies mentioned previously. Many hybrid algorithms discovered in the literature mix rule- and shape-based techniques, which is quite intriguing to observe. However, the ASM-fused approaches have limitations, whereas the form schemes need computing complexity, learning, and training as well as the optimization process.

Watershed algorithm is used for segmentation in some complex images, If we apply simple thresholding and contour detection, then we will not be able to give proper results. The Watershed algorithm is based on extracting sure background and foreground and then using markers will make watershed run and detect the exact boundaries. This algorithm generally helps in detecting touching and overlapping objects in an image.

U-NET architecture (See Figure 2) was originally developed for medical image understanding and segmentation. It has vast applications in the domain and has been a key architecture in the medical imaging automation society. The architecture of this network includes two main parts: contractive and expansive. The contracting path consists of several patches of convolutions with filters of size 3×3 and unity strides in both directions,

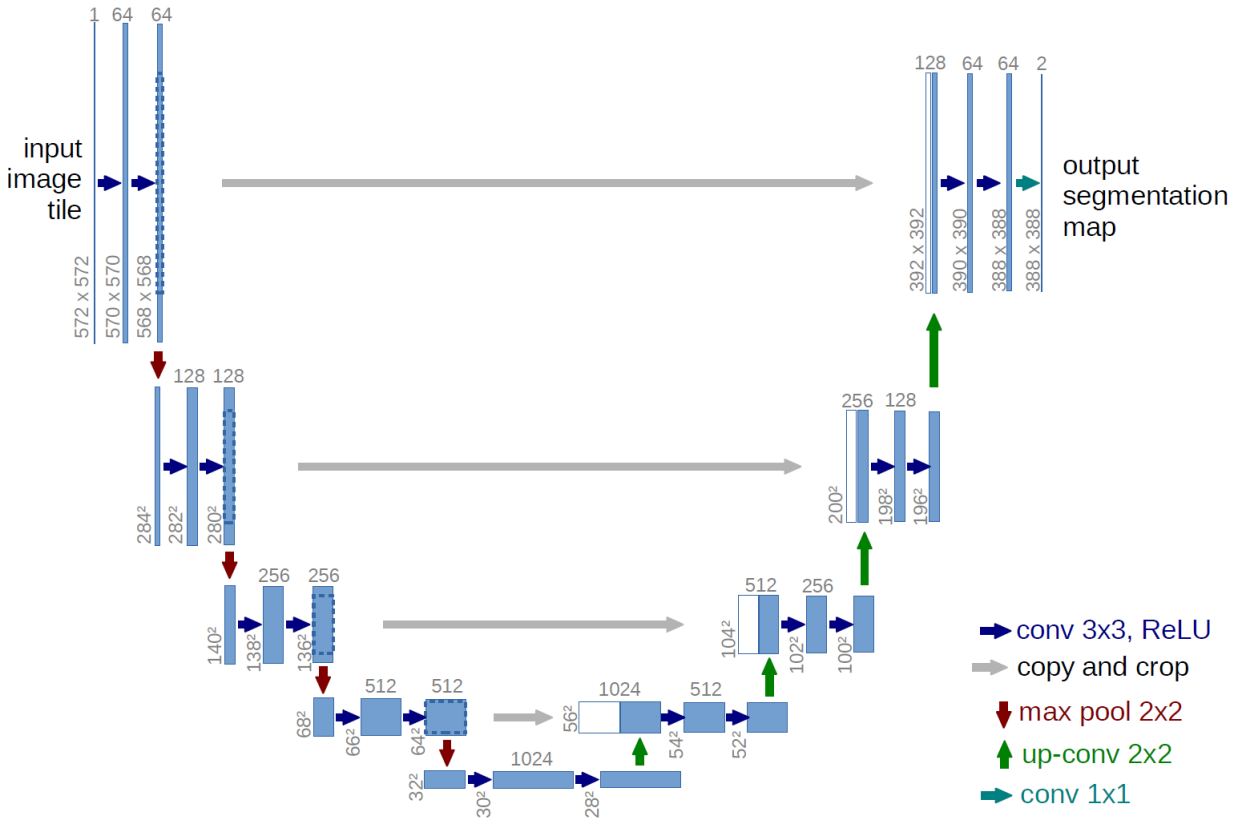

Figure 2: U-Net Architecture [7]

followed by ReLU layers. This path extracts the key features of the input and results in a feature vector of a specific length. The second path pulls information from the contractive path via copying and cropping, and from the feature vector via up-convolutions, and generates, by a successive operation, an output segmentation map. The key component of this architecture is the operation linking the first and second paths together. This linkage allows the network to attain highly accurate information from the contractive path, thus generating the segmentation mask as close as possible to the intended output.

After exploring other deep learning methods like RNN and LSTM, we developed an understanding that since our dataset would contain 2-D X-Ray images, and we would not have any sequential information in any manner, CNN (U-Net) is better choice for our use case of segmentation. Hence, we would not be implementing RNN for image segmentation.

5 Updated Scope of the Study and Tangible Goals

All of us are aware COVID-19 recently affected everyone worldwide with 95,700,347 incident cases with 5,327,014 hospitalizations in united states alone. Tuberculosis and pneumonia are also two highly prevalent disease around the world and lung segmentation could help physicians in early and accurate diagnosis of such diseases and hence could save many lives or reduce the overall healthcare resources by significant margin. By accurately segmenting lungs and identifying boundaries with 100 percent precision, we could feed this data into classification models which can classify patients with tuberculosis with significantly higher accuracy. The scope of this exercise is extended from predicting the segmented mask using traditional and deep learning techniques to eventually using the segmented lung images as an input to predict the presence and absence of tuberculosis

in Shenzhen Hospital X-Ray set. We also evaluated the generalizability of lung segmentation algorithms on Montgomery dataset which were primarily developed for Shenzhen Hospital X-Ray set.

6 Previous work

In previous exercise, we finalized that the algorithms will be developed on Shenzhen dataset and initial data parsing was conducted. We also explored if the data required cleaning, since the images were of high quality no data cleaning was required. We also applied basic traditional methods of thresholding to test the extent of the complex nature of the algorithm required to correctly segment the lungs from the X-ray images. We decided that alone the traditional edge-based method and intensity-based method would not suffice and there was a need to delicately handle and evaluate application and outcome of each traditional method applied. Thus, during the previous submission we started building a U-Net architecture and step wise unsupervised algorithm which uses Watershed technique to predict the mask.
During our previous work we also finalized the evaluation metrics which will be used to comment on success of the segmentation algorithms and further disease classification algorithms. Dice coefficients will be an important metric as it would evaluate the amount of intersecting pixel between ground truth and predicted mask in comparison to all pixels. Recall for disease classification model will be crucial as we would not prefer misidentify patients with the disease. However, other classification metrics will also be evaluated to comment on overall performance of the model.

6.1 Evaluation metrics

6.2 Dice Co-efficient

Dice co-efficient is the size of the overlap of the two segments divided by the total size of the two objects. The Dice coefficient is very similar to the IoU (Intersection over Union). They are positively correlated, meaning if one says model A is better than model B at segmenting an image, then the other will say the same. Like the IoU, they both range from 0 to 1, with 1 signifying the greatest similarity between predicted and truth.

6.3 Other measures

Measures such as sensitivity, specificity, accuracy and overlap score can be computed using these values. In this work, the analyses will be performed to both right and left lungs using the following formulas:

$$Accuracy = (TP + TN)/(TP + TN + FP + FN) \tag{1}$$

$$Sensitivity/Recall(R) = TP/(TP + FN) \tag{2}$$

$$Specificity = TN/(TN + FP) \tag{3}$$

$$Precision(P) = TP/(TP + FP) \tag{4}$$

$$Fscore(F) = 2PRP + R \tag{5}$$

The mentioned metrics were also applied to the classification model for disease classification.

7 Datasets Used

7.1 Shenzhen Chest X-Ray set

The Shenzhen dataset was collected in collaboration with Shenzhen No.3 People's Hospital, Guangdong Medical College, Shenzhen, China. The chest X-rays are from outpatient clinics and were captured as part of the daily hospital routine within a 1-month period, mostly in September 2012, using a Philips DR Digital Diagnostic system. The set contains 662 frontal chest X-rays, of which 326 are normal cases and 336 are cases with manifestations of TB, including pediatric X-rays (AP). The X-rays are provided in PNG format. Their size can vary but is approximately 3K × 3K pixels.
All image file names follow the same template: CHNCXRZZZZZZX, where ZZZZ represents a 4-digit numerical identifier, and X is either 0 for a normal X-ray or 1 for an abnormal X-ray. The clinical reading for each X-ray is saved in a text file following the same format, except that the ending ".png" is replaced with ".txt". Each reading contains the patient's age, gender, and abnormality seen in the lung, if any. However, the patient's characteristics were not used in disease classification model of this study as we wanted to evaluate the marginal effect of segmented mask alone and avoid any interaction with other patient's characteristics.

7.2 Montgomery County chest X-ray set (MC)

This dataset was used to evaluate the generalizability of segmentation algorithm developed on Shenzhen dataset. The MC set has been collected in collaboration with the Department of Health and Human Services, Montgomery County, Maryland, USA. The set contains 138 frontal chest X-rays from Montgomery County's Tuberculosis screening program, of which 80 are normal cases and 58 are cases with manifestations of TB. The X-rays were captured with a Eureka stationary X-ray machine (CR), and are provided in Portable Network Graphics (PNG) format as 12-bit gray level images. They can also be made available in DICOM format upon request. The size of the X-rays is either 4,020×4,892 or 4,892×4,020 pixels.
All image file names follow the same template: MCUCXRZZZZZZZX.png, where ZZZZ represents a 4-digit non-sequential numerical identifier, and X is either 0 for a normal X-ray or 1 for an abnormal X-ray. The clinical reading for each X-ray is saved in a text file following the same format, except that the ending ".png" is replaced with ".txt". Each reading contains the patient's age, gender, and abnormality seen in the lung, if any.
Although, we would have liked to train our model which is more representative of population. In these datasets, nearly 50 percent of patients had Tuberculosis which is not representative of real world and only contains patients from a certain hospital or a county.

8 Approach

We primarily ended up implementing two algorithms for predicting segmentation masks of CXR images – Watershed techniques and U-Net Architecture. The Watershed algorithm was implemented in a step-wise process which involved binary thresholding, background and foreground extraction, marker extraction and eventually the segmented mask (See Figure 3). We also identified that there were many traditional and well regarded methods which didn't work well for this study. For instance, Otsu thresholding didn't work well here and hence we had manually decide the thresholds to do binary thresholding which was one of initial steps in Watershed segmentation pipeline. In our watershed pipeline, at the end all extracted mask were dilated as it was noticed that the process was underestimating the mask size. The abrupt boundaries of extracted mask were also smoothed by the dilation step implemented at the end. The last step of dilation was not required when masks were predicted using U-Net Architecture.

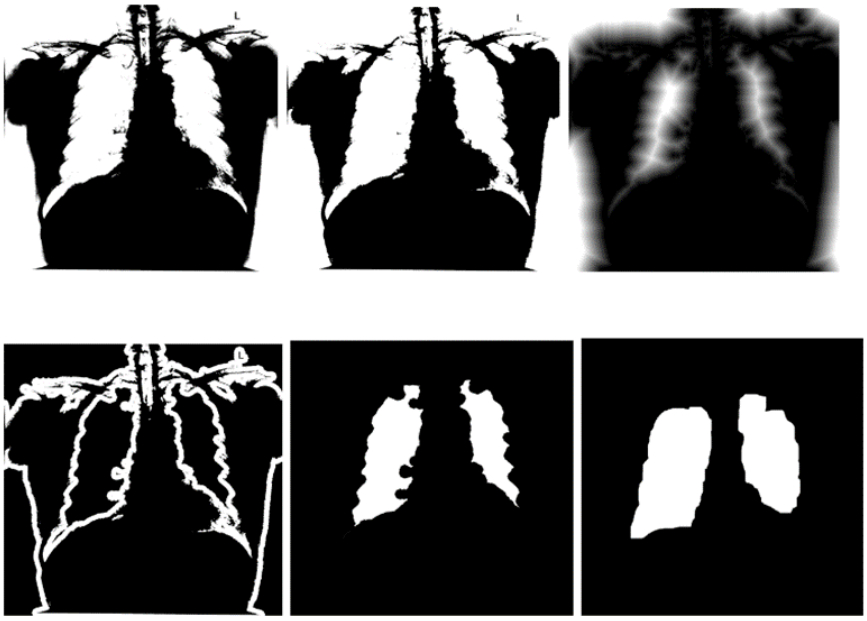

Figure 3: Image outputs through watershed segmentation pipeline including sure background, foreground, markers, distance transforms and segmented mask

Figure 4: Sample of segmented lungs (Inputs to classifier model)

The segmentation algorithm which was developed using Shenzen X-Ray set was also tested on Montgomery dataset. The dice coefficients and pixel wise classification metrics were recorded for resized masks and ground truth.
Once the masks were extracted (See Figure 4) using both segmentation techniques, the masks were used to extract the lungs from the original CXR images. These images were then supplied as an input to the CNN classification model to classify presence/ absence of pulmonary tuberculosis.

9 Results

9.1 Watershed Results

Watershed segmentation technique was able to extract the mask with a dice coefficient of 0.8905 on Shenzhen X-ray set. The images were resized to (256, 256) to calculate the pixel level recall of positive classes as 0.92, precision of 0.88 and F1 score of 0.96. The process was then evaluated on Montgomery dataset to achieve a

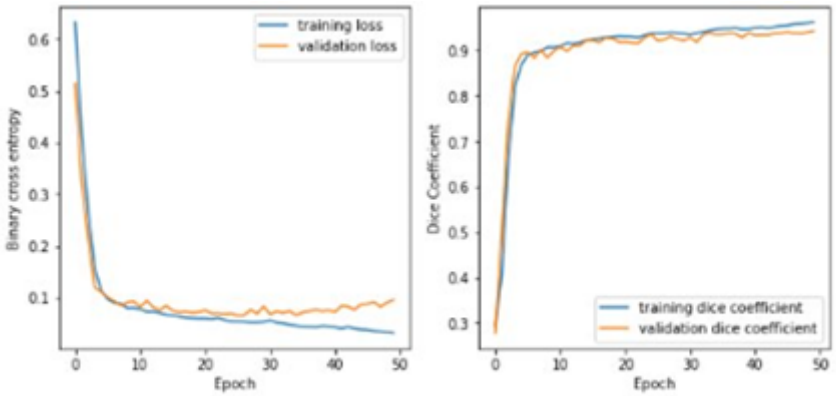

Figure 5: Best Performing model: Loss and Dice coefficient

dice coefficient of 0.9051, with a recall of 0.89, precision of 0.94, F1 score of 0.91 for positive classes on resized images. Please note, the dice coefficients were calculated on original size of ground truth mask and predicted mask.

9.2 U-Net Results

See additonal figure 14 for the model architecture that we have used in order solve the use case of Lung Segmentation in figure 6. Different parameters were tried to reach our best performing model. Below are the few hyper parameters out of all the tried possibilities. With 50 epochs, Adam optimizer and relu activation function we were able to achieve an average dice coefficient of close to 0.95, See Figure 5 and 6. Different parameters were tried to reach our best performing model. See Figure 13 the few hyper parameters out of all the tried possibilities.

9.3 Dice coefficient analysis

The histogram of distribution dice coefficient on our test set explains that majority of the images have dice coefficient of more than 0.90. This explains that the predicted masks exhibit high confidence, See Figure 7

9.4 Tuberculosis classification results using segmented lungs

After accurately segmenting lungs and identifying boundaries, we fed this data into CNN classification models which can classify patients with tuberculosis.Different CNN models were tried starting from a very basic sequential mode containing one convolutional layer followed by a dense layer and prediction.
Later, to improve performance more convolutional layers were added. Max pooling layers and drop out layers were also added. Data augmentation was done by adding horizontal and vertical flips, zoom and rotation (See Figure). Both Adam optimizer and stochastic gradient descent were tried, and their performance were recorded as shown below. Please note initially multi-class classification was attempted with three classes being - “Normal”, “Pulmonary Tuberculosis” and “Other Tuberculosis”. Further, the disease classes were limited to two - “Normal”, “Pulmonary Tuberculosis” as the sample size for “Other Tuberculosis” class was just 10. When CNN classifier was used with stochastic gradient descent as the optimizer, loss function as categorical class entropy, the best performance was achieved. With the final network, we could achieve a recall of 0.74, precision of 0.76 and F1 score of 0.75, see Figure 9 and 10. From the beginning, with an assumption that segmented lung images as input should improve the performance of disease classifier in comparison to complete CXR images as input.

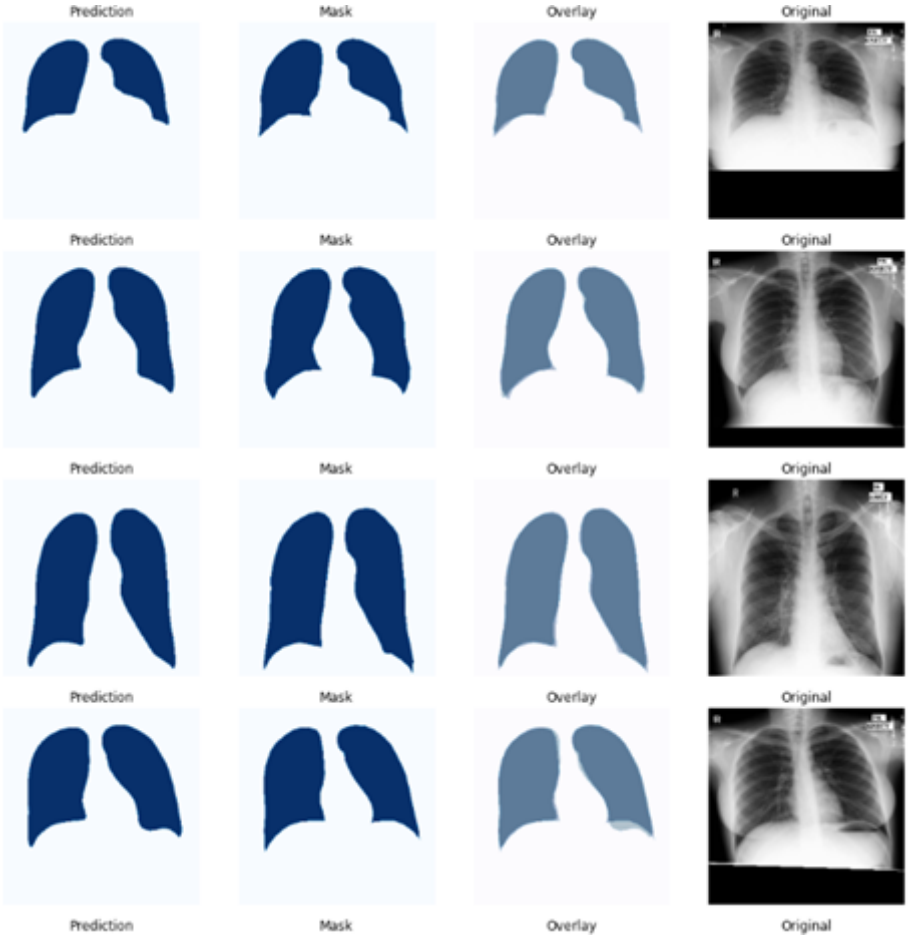

Figure 6: Sample of U-Net results: Prediction, Mask, Overlay and Original image in order from left to right

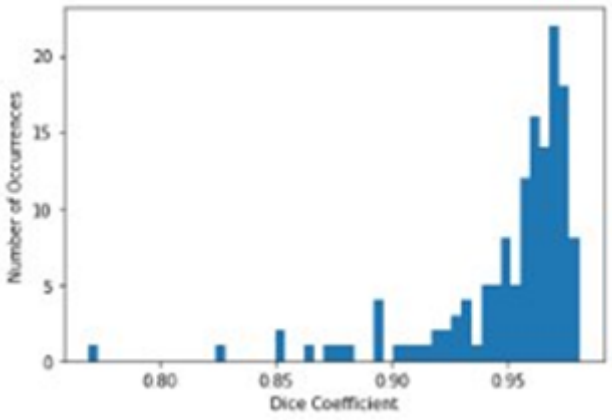

Figure 7: Dice coefficient distribution on test set, U-Net results

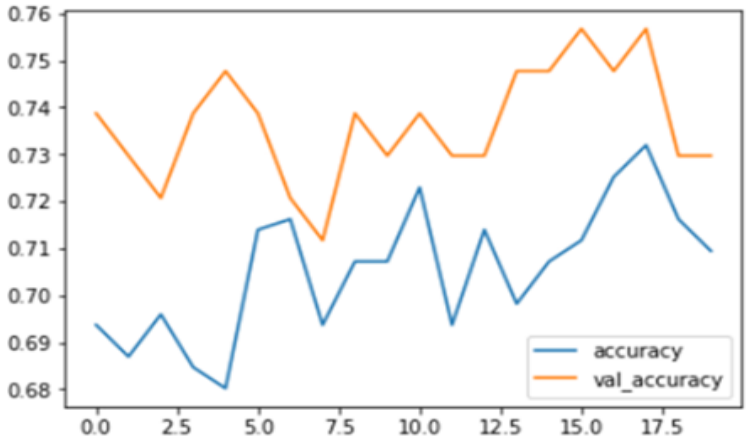

Figure 8: Model performance of initial CNN classifier with no data augmentation and Adam's optimizer

Layer (type)	Output Shape	Param #
sequential_6 (Sequential)	(None, 256, 256, 3)	0
rescaling_3 (Rescaling)	(None, 256, 256, 3)	0
conv2d_5 (Conv2D)	(None, 256, 256, 16)	784
max_pooling2d_3 (MaxPooling 2D)	(None, 128, 128, 16)	0
conv2d_6 (Conv2D)	(None, 128, 128, 32)	8224
max_pooling2d_4 (MaxPooling 2D)	(None, 64, 64, 32)	0
conv2d_7 (Conv2D)	(None, 64, 64, 64)	32832
max_pooling2d_5 (MaxPooling 2D)	(None, 32, 32, 64)	0
dropout_1 (Dropout)	(None, 32, 32, 64)	0
flatten_3 (Flatten)	(None, 65536)	0
dense_6 (Dense)	(None, 128)	8388736
dense_7 (Dense)	(None, 3)	387

Total params: 8,430,963
Trainable params: 8,430,963
Non-trainable params: 0

Figure 9: Final CNN classifier with rescaling, data augmentation, SGD optimizer and Relu activation

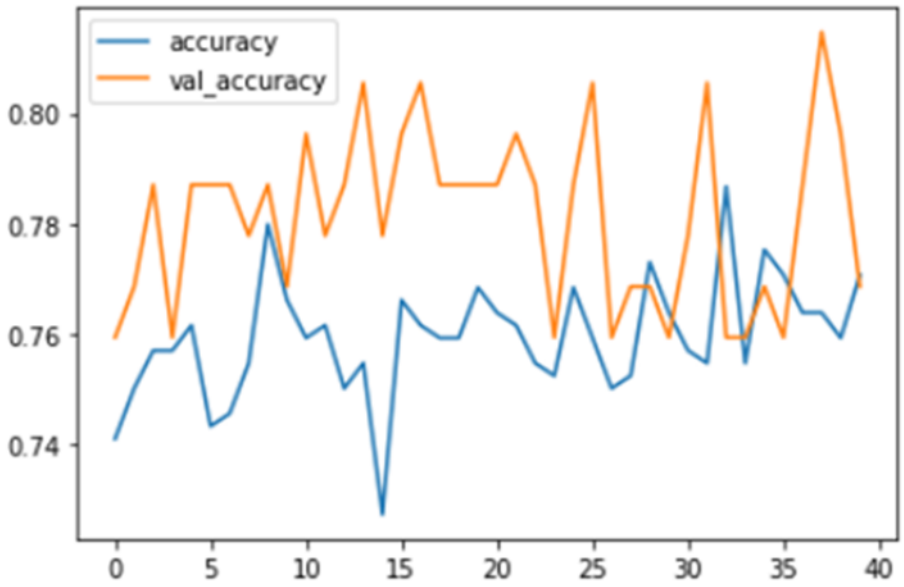

Figure 10: Final model performance of CNN classifier with data augmentation and SGD optimizer

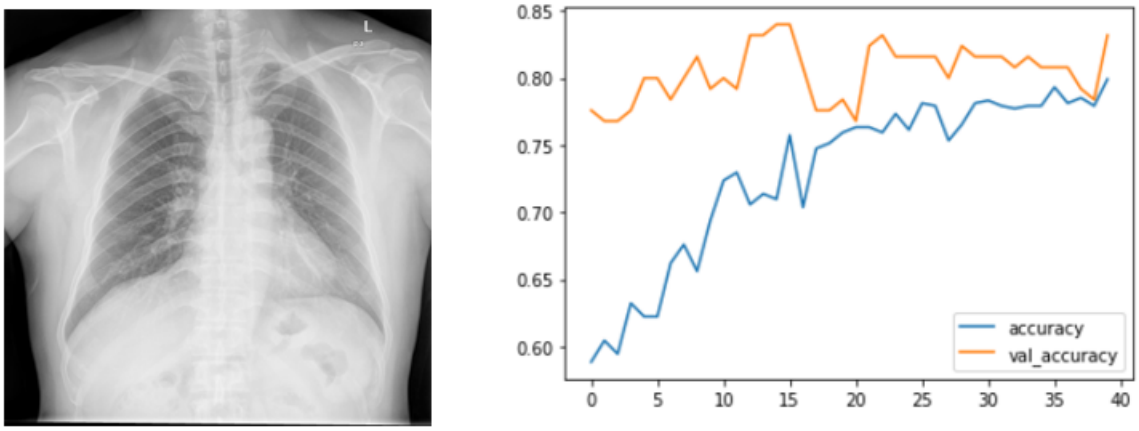

Figure 11: Model performance with complete CXR image as input, on left is the complete CXR image

In the case of segmented images as the input the classifier should be able to train faster and would only have the area of the image which matters, and all the surrounding noise is removed. This motivated us to test the performance of the classifier with original images as input to the classifier. Surprisingly, the CNN classifier worked better with original images as input. The model with original CXR as input achieved a recall of 0.77, precision of 0.87 and F1 score of 0.82, see Figure 11.

9.5 Cross Domain Adaptation

The model was trained on Shenzhen dataset. This model was then tested on the Montgomery dataset to perform the same task. The results were promising. We were able to achieve the dice score of close to 0.93 using U-Net and 0.90 using watershed algorithm. The figure 12 explains the results.

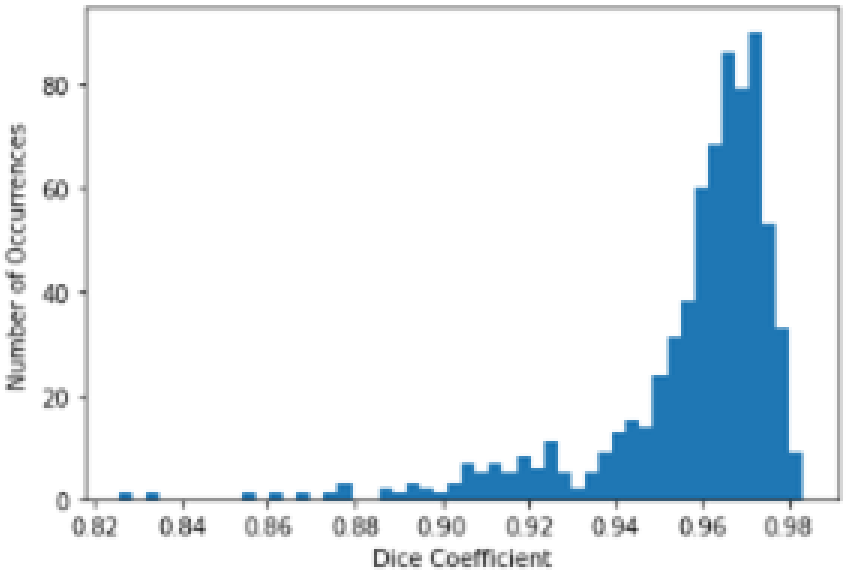

Figure 12: Dice coefficient distribution when tested on Mongtomery set, U-Net results

10 Discussion and Conclusion

The proposed segmentation algorithms worked well with high dice coefficients of 89.05 percent and 94.07 percent using watershed and U-Net Architecture respectively. These segmentation algorithms find its usage in myriad of health science areas. It could help in tracking the health of lungs for a patient over a period of time. Though, the segmentation algorithm worked better for healthy and mild lung conditions, but when this algorithm is implemented on a single patient's CXR images over regular interval it could deliver many fruitful insights to the physician and could help the physician decide a better line of treatment.
In real world applications, the segmented images are considered to be helpful in faster and accurate diagnosis of lung diseases. However, here with segmented images the recall of positive pulmonary tuberculosis was less than when the complete CXR images are used as an input to the disease classifier model. This motivates us to rethink the usage of segmented images in diagnosis of lung diseases. With this study we would like to make a claim that segmentation of lung may not improve the disease classification, but it improves the reliability of results achieved through segmented images.
Our results in the study are subject to small sample size of 550 images out of which 278 were normal and 266 had pulmonary tuberculosis. With a better sample size and deeper network, we may be able to achieve better results. Our results would also depend on the severity of the disease. Minor observations have led us to the conclusion that the classifier may be working for mild patients better than severe patients. A more in-depth medical expertise is required to further comment on such findings. There is a chance that this approach for achieving better classification results may depend on the type of diagnosis itself.

11 Future work

This study could be used as preliminary work to explore further the implication of segmented input into disease identification models for different diagnosis. It would be interesting to explore what precision in diagnosis we can get, if we deploy similar approach for other lung diseases like tumor, pneumonia etc. It would extremely interesting to evaluate this approach with larger sample size and additional covariates like age of patients, gender

of patients, severity of lung disease and other clinical comorbidities. Also, it would be interesting to explore a classifier trained on dataset which is not limited to a certain hospital or region and thus include more robustness into the classifier, unlike this study. Any future work, in collaboration with individuals who have expertise in the domain could lead to uncovering of many interesting insights and eventually help physicians in deciding better line of treatment for a patient in need.

References

[1] Bone shadow eliminated images of the jsrt database. https://www.mit.bme.hu/eng/events/2013/04/18/bone-shadow-eliminated-images-jsrt-database. Accessed: 2022-10-20.

[2] Chest journal. https://journal.chestnet.org/article/S0012-3692(21)04206-9/fulltext. Accessed: 2022-10-20.

[3] Lung disease facts. https://www.cdc.gov/heartdisease/facts.htm. Accessed: 2022-10-20.

[4] Openi - public dataset. https://openi.nlm.nih.gov/faq#faq-tb-coll. Accessed: 2022-10-20.

[5] Segmentation technique. https://www.sciencedirect.com/topics/computer-science/segmentation-technique. Accessed: 2022-10-20.

[6] Tuberclosis. https://www.who.int/news-room/fact-sheets/detail/tuberculosis. Accessed: 2022-10-20.

[7] U-net architecture. https://lmb.informatik.uni-freiburg.de/index.php. Accessed: 2022-10-20.

[8] V7labs - image segmentation technique. https://www.v7labs.com/blog/image-segmentation-guide. Accessed: 2022-10-20.

[9] Baxtyar Ahmed and Muzhir Al-Ani. Digital medical image segmentation using fuzzy c-means clustering. *UHD Journal of Science and Technology*, 4:51, 02 2020.

[10] James Bergstra and Yoshua Bengio. Random search for hyper-parameter optimization. *Journal of machine learning research*, 13(2), 2012.

[11] TF Cootes, MG Roberts, KO Babalola, and CJ Taylor. Active shape and appearance models. In *Handbook of biomedical imaging*, pages 105–122. Springer, 2015.

[12] Shilpa Gite, Abhinav Mishra, and Ketan Kotecha. Enhanced lung image segmentation using deep learning. *Neural Computing and Applications*, pages 1–15, 2022.

[13] Maoguo Gong, Yan Liang, Jiao Shi, Wenping Ma, and Jingjing Ma. Fuzzy c-means clustering with local information and kernel metric for image segmentation. *IEEE Transactions on Image Processing*, 22(2):573–584, 2013.

[14] Maryam Rastgarpour, Jamshid Shanbehzadeh, and Hamid Soltanian-Zadeh. A hybrid method based on fuzzy clustering and local region-based level set for segmentation of inhomogeneous medical images. *Journal of medical systems*, 38(8):68, August 2014.

12 Additional Figures

Below are some additional figures which are referenced in the main text and could provide deeper insights into the work done for this study.

Model	Epochs	Activation Function	Optimizer	Dice Coefficient
UNET	10	tanh	Adagrad	0.68
UNET	20	relu	Adagrad	0.75
UNET	40	tanh	Adagrad	0.71
UNET	40	relu	Adagrad	0.78
UNET	60	relu	Adagrad	0.8
UNET	10	relu	Adadelta	0.72
UNET	20	relu	Adadelta	0.76
UNET	40	leaky relu	Adadelta	0.87
UNET	10	relu	Adam	0.75
UNET	20	relu	Adam	0.86
UNET	40	relu	Adam	0.89
UNET	**50**	**relu**	**Adam**	**0.947**
UNET	60	relu	Adam	0.91

Figure 13: Different U-Net model tried for segmentation

Layer (type)	Output Shape	Param #
input_1 (InputLayer)	[(None, 256, 256, 1)]	0
conv2d (Conv2D)	(None, 256, 256, 32)	320
conv2d_1 (Conv2D)	(None, 256, 256, 32)	9248
max_pooling2d (MaxPooling2D)	(None, 128, 128, 32)	0
conv2d_2 (Conv2D)	(None, 128, 128, 64)	18496
conv2d_3 (Conv2D)	(None, 128, 128, 64)	36928
max_pooling2d_1 (MaxPooling2D)	(None, 64, 64, 64)	0
conv2d_4 (Conv2D)	(None, 64, 64, 128)	73856
conv2d_5 (Conv2D)	(None, 64, 64, 128)	147584
max_pooling2d_2 (MaxPooling2D)	(None, 32, 32, 128)	0
conv2d_6 (Conv2D)	(None, 32, 32, 256)	295168
conv2d_7 (Conv2D)	(None, 32, 32, 256)	590080
max_pooling2d_3 (MaxPooling2D)	(None, 16, 16, 256)	0
conv2d_8 (Conv2D)	(None, 16, 16, 512)	1180160
conv2d_9 (Conv2D)	(None, 16, 16, 512)	2359808
conv2d_transpose (Conv2DTranspose)	(None, 32, 32, 256)	524544
conv2d_10 (Conv2D)	(None, 32, 32, 256)	590080
conv2d_11 (Conv2D)	(None, 32, 32, 256)	590080
conv2d_transpose_1 (Conv2DTranspose)	(None, 64, 64, 128)	131200
conv2d_12 (Conv2D)	(None, 64, 64, 128)	147584
conv2d_13 (Conv2D)	(None, 64, 64, 128)	147584
conv2d_transpose_2 (Conv2DTranspose)	(None, 128, 128, 64)	32832
conv2d_14 (Conv2D)	(None, 128, 128, 64)	36928
conv2d_15 (Conv2D)	(None, 128, 128, 64)	36928
conv2d_transpose_3 (Conv2DTranspose)	(None, 256, 256, 32)	8224
conv2d_16 (Conv2D)	(None, 256, 256, 32)	9248
conv2d_17 (Conv2D)	(None, 256, 256, 32)	9248
conv2d_18 (Conv2D)	(None, 256, 256, 1)	33

Total params: 6,976,161
Trainable params: 6,976,161
Non-trainable params: 0

Figure 14: Final U-Net Architecture used for segmentation